Available online at www.sciencedirect.com
ScienceDirect
Journal of Power Sources 176 (2008) 138–154
JOURNAL OF POWER SOURCES
www.elsevier.com/locate/jpowsour

Short-stack modeling of degradation in solid oxide fuel cells Part I. Contact degradation

J.I. Gazzarri [a], O. Kesler [b,*]

[a] Department of Mechanical Engineering, University of British Columbia, 2054-6250 Applied Science Lane, Vancouver, BC V6T 1Z4, Canada
[b] Department of Mechanical and Industrial Engineering, University of Toronto, 5 King's College Road, Toronto, ON M5S 3G8, Canada

Received 31 August 2007; received in revised form 12 October 2007; accepted 15 October 2007
Available online 23 October 2007

Abstract

As the first part of a two paper series, we present a two-dimensional impedance model of a working solid oxide fuel cell (SOFC) to study the effect of contact degradation on the impedance spectrum for the purpose of non-invasive diagnosis. The two dimensional modeled geometry includes the ribbed interconnect, and is adequate to represent co- and counter-flow configurations. Simulated degradation modes include: cathode delamination, interconnect oxidation, and interconnect-cathode detachment. The simulations show differences in the way each degradation mode impacts the impedance spectrum shape, suggesting that identification is possible. In Part II, we present a sensitivity analysis of the results to input parameter variability that reveals strengths and limitations of the method, as well as describing possible interactions between input parameters and concurrent degradation modes.

Keywords: SOFC; Degradation; Diagnosis; Model; Impedance spectroscopy

1. Introduction

Solid oxide fuel cells (SOFC) are considered a promising candidate to replace thermo-chemical plants based on fossil fuel burning for power generation. Capable of generating electricity with relatively high efficiency, SOFCs are especially suitable for stationary electricity generation. Remote location activities, such as mining, are typical examples of applications in which SOFCs could be useful, providing power in places where access to a distribution grid would be prohibitive in terms of cost.

Despite their advantages, SOFCs have not reached commercial status, due to problems related to durability, reliability, and cost. The importance of the problems associated with durability and reliability is reflected in the significant research effort within the SOFC community aimed at understanding the large number of degradation mechanisms that are known to affect SOFCs. Examples of degradation mechanisms include contact problems between adjacent cell components, microstructural deterioration of the porous electrodes, and blocking of the reaction sites within the electrodes. Contact problems include delamination of an electrode from the electrolyte, growth of a poorly conductive oxide layer between metallic interconnect plates and the electrodes, and lack of contact between one or more interconnect ribs and the electrode, caused, for example, by cell warping prior to stack assembly. Examples of microstructural degradation are anode sintering, carbon deposition, and sulfur or chromium poisoning.

Electrode delamination consists of a detachment of one of the electrodes from the electrolyte. This phenomenon is usually a consequence of thermal or redox cycling, which progressively degrades the bonding of the two adjacent layers at the interface [1–3]. Delamination has severe consequences on the performance, since it increases the ohmic resistance of the cell proportionally to the delaminated area, which impedes the transport of ionic species between the electrode and the electrolyte. Furthermore, it renders the affected area electrochemically inactive as a consequence of the high aspect ratio of the cell, which inhibits the transport of ions in the in-plane directions [4].

The loss of electrochemically active surface area in a porous electrode has a negative impact on cell performance because it causes a decrease in the amount of reaction sites available within the electrode volume. The coarsening of the electrode

* Corresponding author. Tel.: +1 416 978 3835; fax: +1 416 978 7753.
E-mail address: kesler@mie.utoronto.ca (O. Kesler).

0378-7753/$ – see front matter © 2007 Elsevier B.V. All rights reserved.
doi:10.1016/j.jpowsour.2007.10.047

microstructure [5] or the blocking of triple phase boundaries and pores caused by deposits of extraneous elements present in the reactant [6] are common causes of this type of degradation mode.harsh atmospheric conditions on each side of the SOFC interconnect narrow down the spectrum of materials from which to fabricate the cell components to only a few candidates. Expensive lanthanum chromite ceramics are typically used as interconnects in stacks of tubular SOFCs, but cheaper stainless steel interconnects are more commonly used in planar SOFC stacks, thanks to the lower temperature of operation allowed by the planar configuration. Despite their advantages, chromium-based steels oxidize over time under the physical conditions to which they are exposed in an SOFC, and ceramic coatings are often used to slow the rate of oxidation and reduce the rate of chromia evaporation from the interconnects. Scales of chromia grow on the interconnect surface, degrading the electrical conductivity of the interconnect-electrode interface. This oxide layer is dense and adherent, providing the substrate with protection against further oxidation. However, it is important to ensure that the conductivity loss will remain within acceptable limits over the expected lifetime of the fuel cell. Extensive research work on chromia layer growth has focused on the study of oxidation kinetics and on the increase in ohmic resistance over time [7–10]. Park and Natesan [7] studied the kinetics of chromia growth at different temperatures and in different atmospheres. According to their data, it is expected that a 20 μm layer of chromium oxide grows at 850 °C in cathode-like atmospheres over 40,000 h, the current target lifetime for prospective commercial systems for residential applications. Larrain et al. [8] modeled stack degradation derived from interconnect oxidation and anode re-oxidation, analyzing the main factors influencing both processes. According to their model, cells in the inner part of the stack degraded to a larger extent than cells in the outer part, mainly due to temperature differences. Brylewski et al. [9] and Huczkowski et al. [10] conducted similar studies, focusing on SOFC conditions, and leading to similar results. Chen et al. [11] and Huang et al. [12] studied the effectiveness of protective coatings and the oxidation kinetics of 430SS [11] and of a commercial ferritic steel with 26% wt Cr–1% wt Mo [12]. In [11], the authors predicted an increase of approximately 0.5 Ω cm^2 in the area specific resistance of the samples after 50,000 h at 850 °C, using a simple model of the oxide scale geometry.

Solid oxide fuel cell processing routes involve several thermal cycles with temperature changes of the order of 1000–1300 °C. Co-firing and *in situ* firing are examples of techniques aiming at minimizing the number of thermal cycles during manufacture. These thermal excursions, plus those resulting from normal operation, may lead to deformation of the planar cell components, with detrimental consequences associated with contact degradation between the interconnect and the electrodes. If one or more interconnect ribs lose contact with the adjacent electrode, electron conduction will be interrupted through the affected ribs. This phenomenon is referred to as rib detachment [13].

The nature of these degradation mechanisms is very different, and so are their potential corrective actions. Some mechanisms are reversible, and some are irreversible. Therefore, a method to identify individual degradation modes in a non-invasive way would facilitate the identification of those degradation modes that can be reversed or slowed during operation. Currently, the way to identify a given degradation mode is by disassembling the cell for *ex situ* observation and assessment. This method is costly and time consuming, and it requires shutting down the system for extended periods of time. A non-invasive diagnostic technique, on the other hand, would allow reversible degradation modes to be identified and corrected by proper adjustment of the operating variables, and would justify the need to disassemble a stack where an irreversible mode was identified.

A method capable of performing minimally invasive studies of electrochemical systems is impedance spectroscopy. Impedance spectroscopy is commonly used for the study of electrochemical systems, including SOFCs. It consists of observing the current or voltage response of the system to a small sinusoidal perturbation of voltage or current around the operating point. The analysis is performed over a wide range of frequencies, resulting in an impedance spectrum. The impedance spectrum provides information about individual processes that occur simultaneously in the cell, with different time constants. Slow processes such as diffusion cause a phase shift in the impedance response at lower frequencies compared to fast processes such as charge transfer. Therefore, changes in the impedance of an operating SOFC can potentially be linked to individual degradation processes in such a way that they can be uniquely identified.

In earlier studies, we presented a modeling analysis of the influence of electrode delamination [4] and of microstructural degradation modes [14] on the impedance spectrum of an operating SOFC. Those studies suggested several identification strategies for the degradation modes under study. The geometry under study was limited to the cathode–electrolyte–anode system, and the reactant concentration was assumed constant throughout the electrodes, simulating a low fuel utilization scenario. In this work, we extend the modeled system to include the ribbed interconnect plates, and we incorporate the mass balance equations into the system to allow the simulation of variable concentrations of reactants and products through the electrodes. With these additions, the cell-level model can be extended to analyze the impact of contact problems such as interconnect detachment or growth of a lower-conductivity interlayer at the interconnect–electrode interface, on stack performance. Electrode delamination is also revisited for the newly modeled geometry, and mass transport effects on both cell- and stack-level degradation modes have also been examined.

The solution of the mass balance equations improves the predictive capability of the method for larger systems, and it constitutes a necessary stepping-stone toward three dimensional, multi-cell stack simulations. A convenient formulation of the mass balance equations allowed us to solve for the reactant concentration at steady state, and then to solve for the oscillatory components of the concentrations in a linear form. It is also shown how the ribbed interconnect geometry influences the cell impedance due to local reactant depletion underneath the ribs, resulting in concentration polarization occurring at current densities far below the mass transport limitation regime.

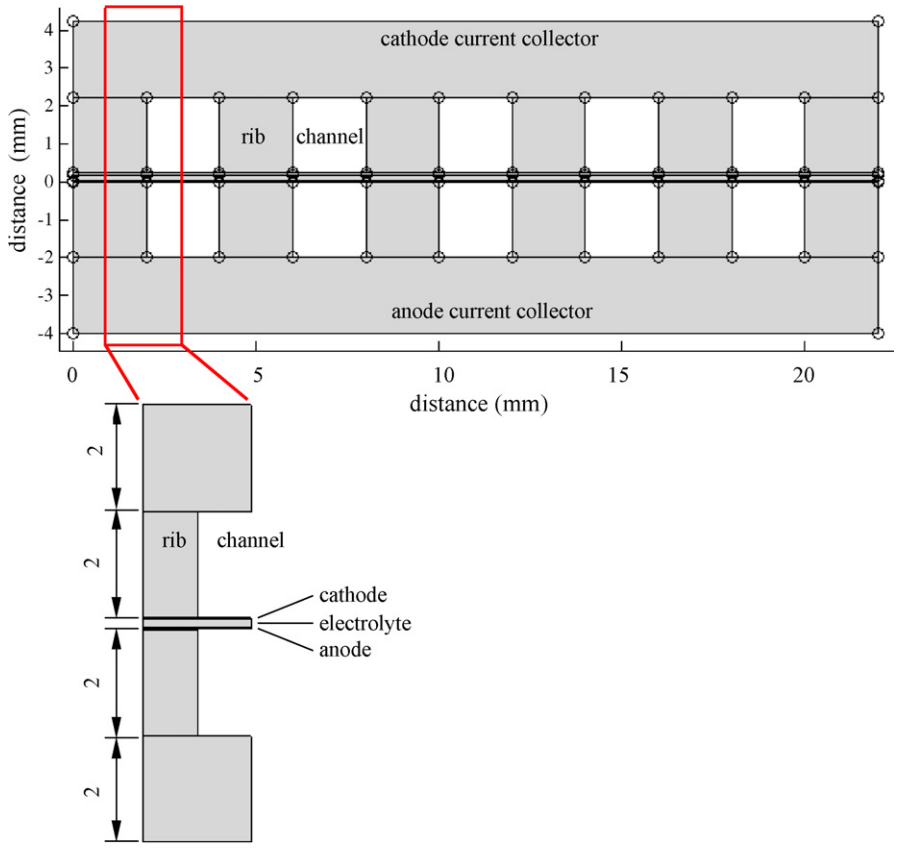

Fig. 1. The geometry including the ribbed interconnect plates. This two-dimensional approximation is valid for co- and counter-flow configurations. The repeating unit geometry represented by half a rib and half a channel is useful to represent the intact case and degradation modes that affect the cell uniformly, such as interconnect oxidation.

2. Numerical model

2.1. Geometry

The modeled geometry is, at present, restricted to two dimensions. With this simplification, the influence of reactant dilution along the channel can be modeled only by the consideration of 2-dimensional cross-sections representing different locations along the channel, with different concentrations at the channel–electrode interface occurring at each section. The influence of changes in reactant concentration along the channel length is accounted for in Part II of this series, in the multivariable parametric study, by parameterizing the inlet concentration and allowing it to vary over a broad range from low to high fuel and oxidant utilizations. Furthermore, the model represents the situation at a section of either a co- or counter-flow stack. Cross flow, an inherently three-dimensional geometry, cannot be represented using a two-dimensional model. Fig. 1 shows the six-rib geometry as generated by the finite element package. A repeating unit consisting of half of a rib width and half of a channel width represents the behavior of the intact cell if used with the appropriate symmetry boundary conditions. However, this approach is not useful to simulate localized degradation phenomena such as delamination or interconnect detachment, because these modes destroy the cell symmetry. The simplified repeating unit approach is useful to simulate oxide layer growth, under the assumption that the oxide layer appears on all ribs uniformly. The intact cases corresponding to the repeating unit and the complete geometry are not identical because of end effects that appear in the six-rib configuration.

2.2. Model equations

Several phenomena take place simultaneously within a working SOFC. The reactants flow along the interconnect channel and diffuse into the porous electrode toward the electrolyte, driven by the concentration gradient established due to electrochemical consumption. A result of this reaction is the production or consumption of ionic or electronic species, which move along the ionically or electronically conductive phase. Furthermore, there is production or consumption of heat, depending on the type of chemical or electrochemical reaction taking place within the porous electrode. In our present study, we restrict the model to the solution of the mass and charge transport equations within the electrodes, the electrolyte, and the interconnect, and we consider only the electrochemical oxidation of hydrogen fuel by oxygen from the air.

The general equation for the conservation of species x is

$$\frac{\partial x}{\partial t} = -\nabla \cdot \underline{N}_x + R_x \tag{1}$$

This equation indicates that the accumulation of species x with time t, $\partial x/\partial t$, is given by the negative divergence of the flux N_x of x plus the volumetric production or consumption of x, R_x. This general equation will be used in the form of mass and charge conservation equations to solve for potentials and concentrations throughout the cell components. For example, if x represents ionic or electronic charge per unit volume ($\mathrm{C\,m^{-3}}$), N_x will represent a current density, and R_x will take the form of a Faradaic current source or sink. If the fundamental variable to be solved is electric potential, the accumulation term will describe the charge of an interfacial double layer, given by a time change in potential. The current density will be expressed as proportional to a gradient in potential using Ohm's law. If x represents concentration of gaseous species within the electrode pores ($\mathrm{mol\,m^{-3}}$), N_x will become a diffusive mass flux, and R_x will take the form of a Faradaic production or consumption of gas species.

The DC and AC sets of equations for the charge transport have been described in detail previously [4], with the influence of concentration gradients neglected. This work presents both the DC and the time-independent approximations of the AC diffusion equations. The latter are linearized around an operating point, thus allowing the solution of a linear set of AC equations, superimposed on a DC solution found earlier and independently. A further addition to the previous model is the coupling between charge and mass balance, i.e. the incorporation of concentration polarization effects in the charge transport equations.

2.2.1. Steady-state equations

2.2.1.1. DC charge transport including coupling with mass transport. A detailed explanation of the charge balance equations has been presented previously [4], under the assumption of no mass transport limitations. The general form of the ionic or electronic charge balance for an elemental volume within a porous electrode is:

$$-SC_{dl}\frac{\partial \eta}{\partial t} = -\nabla \cdot i + Si_{\mathrm{F}}(\eta), \tag{2}$$

Expressions (3)–(6) below show examples of the DC charge balance equations used in the present work. The concentration ratios affecting the exponential terms in the Butler–Volmer expression link the charge and mass transfer processes. The addition of these terms constitutes an upgrade with respect to our previous contribution, and it is the mechanism by which concentration polarization is included in the present model.

The ionic charge balance equation at the cathode modified to include the concentration effects is:

$$-k_{\mathrm{ION,CAT}}\nabla^2\Phi_{\mathrm{ION}} = S_{\mathrm{CAT}}i_{0,\mathrm{CAT}}\left[\exp\left(\frac{\alpha_{\mathrm{CAT,ANO}}F}{RT}\eta_{\mathrm{CAT}}\right) - \frac{c_{\mathrm{O_2}}}{c^0_{\mathrm{O_2}}}\exp\left(-\frac{\alpha_{\mathrm{CAT,CAT}}F}{RT}\eta_{\mathrm{CAT}}\right)\right] \tag{3}$$

where $i_{0,\mathrm{CAT}}$ is the cathodic exchange current density ($\mathrm{A\,m^{-2}}$), α_{ij} is the charge transfer coefficient for the reaction, with the first sub-index indicating the electrode and the second sub-index indicating the anodic or cathodic direction, F is the Faraday's constant ($\mathrm{A\,s\,mol^{-1}}$), R is the universal gas constant ($\mathrm{J\,mol^{-1}\,K^{-1}}$), T is the absolute temperature (K), $c_{\mathrm{O_2}}$ ($\mathrm{mol\,m^{-3}}$) is the local oxygen concentration, and $c^0_{\mathrm{O_2}}$ ($\mathrm{mol\,m^{-3}}$) is the reference oxygen concentration at which $i_{0,\mathrm{CAT}}$ is measured and is coincident with the channel concentration in this work.

The ionic charge balance at the anode with concentration effects included is:

$$-k_{\mathrm{ION,ANO}}\nabla^2\Phi_{\mathrm{ION}} = S_{\mathrm{ANO}}i_{0,\mathrm{ANO}}\left[\frac{c_{\mathrm{H_2}}}{c^0_{\mathrm{H_2}}}\exp\left(\frac{\alpha_{\mathrm{ANO,ANO}}F}{RT}\eta_{\mathrm{ANO}}\right) - \frac{c_{\mathrm{H_2O}}}{c^0_{\mathrm{H_2O}}}\exp\left(-\frac{\alpha_{\mathrm{ANO,CAT}}F}{RT}\eta_{\mathrm{ANO}}\right)\right] \tag{4}$$

The electronic charge balance equations at the cathode and the anode are obtained in a similar way, using the proper conductivities of the media, and inverting the sign of the source term with respect to their ionic counterparts [4].

At the electrolyte, the ionic potential follows:

$$\nabla^2\Phi_{\mathrm{ION}} = 0 \tag{5}$$

At the interconnect, the electronic potential obeys:

$$\nabla^2\Phi_{\mathrm{ELE}} = 0 \tag{6}$$

Prescribed potential boundary conditions for the steady state equations are only required for the electronic potential, along the current collecting lines at the top of the cathode interconnect and at the bottom of the anode interconnect:

$$\begin{aligned}\Phi_{\mathrm{ELE}}|_{\text{cathode current collector}} &= V_{\mathrm{CELL}}\\ \Phi_{\mathrm{ELE}}|_{\text{anode current collector}} &= 0\end{aligned} \tag{7}$$

2.2.1.2. DC mass transport. The reactant flows within a porous electrode are driven by a concentration gradient established between the boundaries with the channel and with the electrolyte. The change in reactant or product concentration at a point within an electrode is proportional to the divergence of the negative flux of that species, and to the electrochemical production or consumption.

$$\frac{\partial c_k}{\partial t} = -\nabla \cdot N_k + \frac{Si_{\mathrm{F}}(\eta)}{nF} \tag{8}$$

Here, c_k is the concentration of species k ($\mathrm{mol\,m^{-3}}$), and N_k is the species' molar flux ($\mathrm{mol\,s^{-1}\,m^{-2}}$), n is the number of electrons participating in the relevant electrochemical production or consumption reaction, and the other terms are as defined above. Eq. (8) indicates that accumulation of species within a volume element can be the result of diffusive flux and of electrochemical production or consumption. For binary gas mixtures, Fick's law of diffusion gives an adequate representation of the diffusive flux, under the assumption that Knudsen

diffusion effects are small for pore sizes of about 1 μm and larger [15]:

$$N_k = -D_k \nabla c_k + x_k N_{\mathrm{TOT}}, \tag{9}$$

where D_k is the effective diffusivity of the gas in the binary mixture, x_k is the molar fraction of species k, and N_{TOT} is the total flux for all species [16].

At the anode, hydrogen diffuses toward the electrolyte, while gaseous water diffuses away from it. This combination obeys the laws of binary equimolar diffusion, since the sum of molar hydrogen and water fluxes is null at every point because every hydrogen molecule that reacts is transformed into a water molecule:

$$N_{\mathrm{TOT}} = N_{\mathrm{H_2}} + N_{\mathrm{H_2O}} = 0 \tag{10}$$

$$N_{\mathrm{H_2}} = -D_{\mathrm{H_2-H_2O}} \nabla c_{\mathrm{H_2}} \tag{11}$$

The following steady-state mass balance equation for the hydrogen at the anode results, assuming that the effective diffusion coefficient is spatially invariant, i.e., that the porosity and microstructure are invariant throughout the electrode:

$$-D_{\mathrm{H_2-H_2O}} \nabla^2 c_{\mathrm{H_2}} = -\frac{S_{\mathrm{ANO}} i_{0,\mathrm{ANO}}}{2F} \left[\frac{c_{\mathrm{H_2}}}{c^0_{\mathrm{H_2}}} \exp\left(\frac{\alpha_{\mathrm{ANO,ANO}} F}{RT} \eta_{\mathrm{ANO}} \right) - \frac{c_{\mathrm{H_2O}}}{c^0_{\mathrm{H_2O}}} \exp\left(-\frac{\alpha_{\mathrm{ANO,CAT}} F}{RT} \eta_{\mathrm{ANO}} \right) \right] \tag{12}$$

For a full cell in which a bi-layered electrode structure is used to optimize the electrochemical and mass transport properties, the electrode would be represented by 2 separate domains in the model geometry. Eq. (12) would be solved in each domain, using the appropriate effective diffusivity for each layer of the electrode.

The water concentration is calculated using the relation:

$$x_{\mathrm{H_2}} + x_{\mathrm{H_2O}} = 1, \tag{13}$$

with x_k indicating the molar fraction of species k.

At the cathode the situation is slightly different, since only oxygen takes part in the reaction of the two primary gas phase species, while the nitrogen in the cathode remains unreacted. The net total flux at a reaction site is therefore equal to the net oxygen flux, since the net flux of nitrogen at any specific reaction site is null:

$$N_{\mathrm{O_2}} = -D_{\mathrm{O_2-N_2}} \nabla c_{\mathrm{O_2}} + x_{\mathrm{O_2}} N_{\mathrm{O_2}} \tag{14}$$

Simplifying and substituting for the mole fraction $x_{\mathrm{O_2}}$ from the ideal gas law,

$$N_{\mathrm{O_2}} = \frac{-D_{\mathrm{O_2-N_2}} \nabla c_{\mathrm{O_2}}}{1 - x_{\mathrm{O_2}}} = \frac{-D_{\mathrm{O_2-N_2}} \nabla c_{\mathrm{O_2}}}{1 - (RT/P) c_{\mathrm{O_2}}}, \tag{15}$$

where p is the total pressure of the system, often very close to atmospheric pressure. The resulting mass transport equation, again assuming that the diffusivity is spatially invariant, is:

$$-D_{\mathrm{O_2-N_2}} \nabla \cdot \left(\frac{\nabla c_{\mathrm{O_2}}}{1 - (RT/p) c_{\mathrm{O_2}}} \right) = \frac{S_{\mathrm{CAT}} i_{0,\mathrm{CAT}}}{4F} \left[\exp\left(\frac{\alpha_{\mathrm{CAT,ANO}} F}{RT} \eta_{\mathrm{CAT}} \right) - \frac{c_{\mathrm{O_2}}}{c^0_{\mathrm{O_2}}} \exp\left(-\frac{\alpha_{\mathrm{CAT,CAT}} F}{RT} \eta_{\mathrm{CAT}} \right) \right] \tag{16}$$

The boundary conditions for hydrogen and oxygen concentrations are prescribed concentrations at the boundaries between the electrodes and channels, and no-flux everywhere else:

$c_{\mathrm{H_2}} = c^0_{\mathrm{H_2}}$ $c_{\mathrm{H_2O}} = c^0_{\mathrm{H_2O}}$	at the channel/anode boundary
$\nabla c_{\mathrm{H_2}} \cdot n = 0$ $\nabla c_{\mathrm{H_2O}} \cdot n = 0$	everywhere else on the anode side
$c_{\mathrm{O_2}} = c^0_{\mathrm{O_2}}$	at the channel/cathode boundary
$\nabla c_{\mathrm{O_2}} \cdot n = 0$	everywhere else on the cathode side

The DC mass transport equations are solved within the porous electrodes, simultaneously with the DC charge transport equations. The equations are nonlinear and coupled. The nonlinearity arises from the exponential dependence of current density on overpotential. The coupling is a result of the concentration dependence of the Butler–Volmer source terms. Comsol Multiphysics (Comsol, Inc.) general purpose PDE solver was used to solve the equations using finite elements. The choice of initial guess is of importance to achieve convergence. The default value for the initial guess is zero for the COMSOL package, but a better value is the Dirichlet boundary condition value.

2.2.2. AC equations

2.2.2.1. AC charge transport. The time dependent transport Eq. (2) can be transformed into complex-valued, time independent equations, by assuming that the response to a small sinusoidal perturbation is also sinusoidal, of the same frequency as the perturbation, and can be decoupled into a DC component and a small sinusoidal component superimposed on it [4]. A limitation of this earlier formulation is that it ignored concentration gradients. In this work, mass transport and concentration gradients are considered, and all unknown functions are decomposed into a steady state and an oscillatory component, under the assumption of small perturbation and linear response of the system around the steady state point:

$$\begin{aligned} \Phi_{\mathrm{ELE}} &= \bar{\Phi}_{\mathrm{ELE}} + \tilde{\Phi}_{\mathrm{ELE}} \, \mathrm{e}^{\mathrm{j}\omega t} \\ \Phi_{\mathrm{ION}} &= \bar{\Phi}_{\mathrm{ION}} + \tilde{\Phi}_{\mathrm{ION}} \, \mathrm{e}^{\mathrm{j}\omega t} \\ c_{\mathrm{H_2}} &= \bar{c}_{\mathrm{H_2}} + \tilde{c}_{\mathrm{H_2}} \, \mathrm{e}^{\mathrm{j}\omega t} \\ c_{\mathrm{O_2}} &= \bar{c}_{\mathrm{O_2}} + \tilde{c}_{\mathrm{O_2}} \, \mathrm{e}^{\mathrm{j}\omega t} \\ c_{\mathrm{H_2O}} &= \bar{c}_{\mathrm{H_2O}} + \tilde{c}_{\mathrm{H_2O}} \, \mathrm{e}^{\mathrm{j}\omega t} \end{aligned} \tag{17}$$

The oscillatory component is a complex variable of small magnitude that represents the phase shift and the excursion from the equilibrium point of the corresponding variable. The

magnitude of the oscillatory component of the electronic potentials ranges between zero and the imposed AC potential, 20 mV in this example. According to our calculations, the oscillatory components of the concentrations are of the order of 10^{-1} mol m^{-3} for low frequencies, and range down to values as low as 10^{-10} mol m^{-3} for the maximum frequency.[1]

Taking the anode ionic charge transport as a working example, the expressions above are substituted into Eq. (2):

$$-S_{\mathrm{ANO}}C_{dl,\mathrm{ANO}}\frac{\partial}{\partial t}(\bar{\eta}+\tilde{\eta}\,\mathrm{e}^{\mathrm{j}\omega t})-k_{\mathrm{ION,ANO}}\nabla^2(\bar{\Phi}_{\mathrm{ION}}+\tilde{\Phi}_{\mathrm{ION}}\,\mathrm{e}^{\mathrm{j}\omega t}) = S_{\mathrm{ANO}}i_{0,\mathrm{ANO}}\left[\frac{\bar{c}_{\mathrm{H_2}}+\tilde{c}_{\mathrm{H_2}}\,\mathrm{e}^{\mathrm{j}\omega t}}{c^0_{\mathrm{H_2}}}\exp(f_{\mathrm{aa}}(\bar{\eta}+\tilde{\eta}\,\mathrm{e}^{\mathrm{j}\omega t}))-\frac{\bar{c}_{\mathrm{H_2O}}+\tilde{c}_{\mathrm{H_2O}}\,\mathrm{e}^{\mathrm{j}\omega t}}{c^0_{\mathrm{H_2O}}}\exp(-f_{\mathrm{ac}}(\bar{\eta}+\tilde{\eta}\,\mathrm{e}^{\mathrm{j}\omega t}))\right] \tag{18}$$

Here, for notation simplicity, we have made the following replacements:

$$\begin{aligned}\bar{\eta} &= \bar{\Phi}_{\mathrm{ELE}}-\bar{\Phi}_{\mathrm{ION}}-\Phi_{\mathrm{REF}}\\ \tilde{\eta} &= \tilde{\Phi}_{\mathrm{ELE}}-\tilde{\Phi}_{\mathrm{ION}}\\ f_{\mathrm{aa}} &= \frac{\alpha_{\mathrm{ANO,ANO}}F}{RT}\\ f_{\mathrm{ac}} &= \frac{\alpha_{\mathrm{ANO,CAT}}F}{RT}\end{aligned} \tag{19}$$

Eq. (18) contains terms that can be expressed in simpler form, on account of the small amplitude of the perturbation:

$$\begin{aligned}\exp(f_{\mathrm{aa}}(\bar{\eta}+\tilde{\eta}\,\mathrm{e}^{\mathrm{j}\omega t}))&\approx\exp(f_{\mathrm{aa}}\bar{\eta})(1+f_{\mathrm{aa}}\tilde{\eta}\,\mathrm{e}^{\mathrm{j}\omega t})\\ \exp(-f_{\mathrm{ac}}(\bar{\eta}+\tilde{\eta}\,\mathrm{e}^{\mathrm{j}\omega t}))&\approx\exp(-f_{\mathrm{ac}}\bar{\eta})(1-f_{\mathrm{ac}}\tilde{\eta}\,\mathrm{e}^{\mathrm{j}\omega t})\end{aligned} \tag{20}$$

Substituting Eq. (20) in (18) and expanding the time derivative,

$$\begin{aligned}&-S_{\mathrm{ANO}}C_{\mathrm{dl,ANO}}\mathrm{j}\omega\tilde{\eta}\,\mathrm{e}^{\mathrm{j}\omega t}-k_{\mathrm{ION,ANO}}\nabla^2\tilde{\Phi}_{\mathrm{ION}}\\ &\quad-k_{\mathrm{ION,ANO}}\,\mathrm{e}^{\mathrm{j}\omega t}\nabla^2\tilde{\Phi}_{\mathrm{ION}}=S_{\mathrm{ANO}}i_{0,\mathrm{ANO}}\\ &\quad\times\left[\begin{array}{l}\dfrac{\bar{c}_{\mathrm{H_2}}}{c^0_{\mathrm{H_2}}}\exp(f_{\mathrm{aa}}\bar{\eta})-\dfrac{\bar{c}_{\mathrm{H_2O}}}{c^0_{\mathrm{H_2O}}}\exp(-f_{\mathrm{ac}}\bar{\eta})+\\ \dfrac{\bar{c}_{\mathrm{H_2}}}{c^0_{\mathrm{H_2}}}\exp(f_{\mathrm{aa}}\bar{\eta})f_{\mathrm{aa}}\,\mathrm{e}^{\mathrm{j}\omega t}\tilde{\eta}+\dfrac{\bar{c}_{\mathrm{H_2O}}}{c^0_{\mathrm{H_2O}}}\\ \quad\exp(-f_{\mathrm{ac}}\bar{\eta})f_{\mathrm{ac}}\,\mathrm{e}^{\mathrm{j}\omega t}\tilde{\eta}+\\ \dfrac{\tilde{c}_{\mathrm{H_2}}}{c^0_{\mathrm{H_2}}}\exp(f_{\mathrm{aa}}\bar{\eta})\,\mathrm{e}^{\mathrm{j}\omega t}-\dfrac{\tilde{c}_{\mathrm{H_2O}}}{c^0_{\mathrm{H_2O}}}\exp(-f_{\mathrm{ac}}\bar{\eta})\,\mathrm{e}^{\mathrm{j}\omega t}+\\ \dfrac{\tilde{c}_{\mathrm{H_2}}}{c^0_{\mathrm{H_2}}}\,\mathrm{e}^{\mathrm{j}\omega t}\exp(f_{\mathrm{aa}}\bar{\eta})\,\mathrm{e}^{\mathrm{j}\omega t}f_{\mathrm{aa}}\tilde{\eta}+\dfrac{\tilde{c}_{\mathrm{H_2O}}}{c^0_{\mathrm{H_2O}}}\,\mathrm{e}^{\mathrm{j}\omega t}\\ \times\exp(-f_{\mathrm{ac}}\bar{\eta})\,\mathrm{e}^{\mathrm{j}\omega t}f_{\mathrm{ac}}\tilde{\eta}\end{array}\right]\end{aligned} \tag{21}$$

All terms in Eq. (21) that do not have $\mathrm{e}^{\mathrm{j}\omega t}$ as a factor cancel out because they are identical to those of the steady state equation, whose solution we already have (Eq. (4)). Furthermore, the last two terms in brackets are of second order, since they contain the product of two oscillatory terms, $\tilde{c}_{\mathrm{H_2}}\tilde{\eta}$ and $\tilde{c}_{\mathrm{H_2O}}\tilde{\eta}$, each of small magnitude, and can therefore be neglected with respect to the other terms. These two simplifications allow the removal of the $\mathrm{e}^{\mathrm{j}\omega t}$ term from all the remaining terms, yielding a *linear, time independent* PDE with respect to the oscillatory potential and concentration amplitudes [17]:

$$\begin{aligned}&-S_{\mathrm{ANO}}C_{\mathrm{dl,ANO}}\mathrm{j}\omega\tilde{\eta}-k_{\mathrm{ION,ANO}}\nabla^2\tilde{\Phi}_{\mathrm{ION}}\\ &\quad=S_{\mathrm{ANO}}i_{0,\mathrm{ANO}}\left[\frac{\bar{c}_{\mathrm{H_2}}}{c^0_{\mathrm{H_2}}}\exp(f_{\mathrm{aa}}\bar{\eta})f_{\mathrm{aa}}\tilde{\eta}+\frac{\bar{c}_{\mathrm{H_2O}}}{c^0_{\mathrm{H_2O}}}\exp(-f_{\mathrm{ac}}\bar{\eta})f_{\mathrm{ac}}\tilde{\eta}\right.\\ &\qquad\left.+\frac{\tilde{c}_{\mathrm{H_2}}}{c^0_{\mathrm{H_2}}}\exp(f_{\mathrm{aa}}\bar{\eta})-\frac{\tilde{c}_{\mathrm{H_2O}}}{c^0_{\mathrm{H_2O}}}\exp(-f_{\mathrm{ac}}\bar{\eta})\right]\end{aligned} \tag{22}$$

The first two terms in the brackets correspond to the Faradaic local current that appears as a consequence of the imposed AC overpotential $\tilde{\eta}$. The last two terms in the brackets indicate the AC concentration contribution to the source term. This formulation is numerically very convenient, since the DC component of the solution is decoupled from the AC component of the solution. On account of the small size of the AC perturbation, it does not have any influence on the DC solution. This fact allows the solution of the AC equations based on the previously and independently obtained DC solution. The steady-state equations are solved using a nonlinear iterative routine yielding values for $\bar{\eta}$ and $\bar{c}$, and the steady state solution is then used as a base on which the AC solution is superimposed. No iterative method is required for the latter, since the equations are linear in the oscillatory unknowns. The electronic potential equation is obtained similarly, resulting in:

$$\begin{aligned}&-S_{\mathrm{ANO}}C_{\mathrm{dl,ANO}}\mathrm{j}\omega\tilde{\eta}-k_{\mathrm{ELE,ANO}}\nabla^2\tilde{\Phi}_{\mathrm{ELE}}=-S_{\mathrm{ANO}}i_{0,\mathrm{ANO}}\\ &\quad\times\left[\frac{\bar{c}_{\mathrm{H_2}}}{c^0_{\mathrm{H_2}}}\exp(f_{\mathrm{aa}}\bar{\eta})f_{\mathrm{aa}}\tilde{\eta}+\frac{\bar{c}_{\mathrm{H_2O}}}{c^0_{\mathrm{H_2O}}}\exp(-f_{\mathrm{ac}}\bar{\eta})f_{\mathrm{ac}}\tilde{\eta}\right.\\ &\qquad\left.+\frac{\tilde{c}_{\mathrm{H_2}}}{c^0_{\mathrm{H_2}}}\exp(f_{\mathrm{aa}}\bar{\eta})-\frac{\tilde{c}_{\mathrm{H_2O}}}{c^0_{\mathrm{H_2O}}}\exp(-f_{\mathrm{ac}}\bar{\eta})\right]\end{aligned} \tag{23}$$

The derivation of the cathode ionic charge balance equation is omitted, but it is obtained in the same way, resulting in:

$$\begin{aligned}&-S_{\mathrm{CAT}}C_{\mathrm{dl,CAT}}\mathrm{j}\omega\tilde{\eta}-k_{\mathrm{ION,CAT}}\nabla^2\tilde{\Phi}_{\mathrm{ION}}\\ &\quad=S_{\mathrm{CAT}}i_{0,\mathrm{CAT}}\left[\exp(f_{\mathrm{ca}}\bar{\eta})f_{\mathrm{ca}}\tilde{\eta}+\frac{\bar{c}_{\mathrm{O_2}}}{c^0_{\mathrm{O_2}}}\exp(-f_{\mathrm{cc}}\bar{\eta})f_{\mathrm{cc}}\tilde{\eta}\right.\\ &\qquad\left.-\frac{\tilde{c}_{\mathrm{O_2}}}{c^0_{\mathrm{O_2}}}\exp(-f_{\mathrm{cc}}\bar{\eta})\right]\end{aligned} \tag{24}$$

[1] An intuitive way to understand this behaviour is by thinking of the solution of the diffusion equation along a semi-infinite 1D domain, imposing an oscillatory boundary condition at the origin. The penetration of the oscillation decreases with increasing perturbation frequency for a fixed diffusivity.

Finally, a similar expression corresponds to the electronic charge balance at the cathode:

$$-S_{CAT}C_{dl,CAT}j\omega\tilde{\eta} - k_{ELE,CAT}\nabla^2\tilde{\Phi}_{ELE} = -S_{CAT}i_{0,CAT}\left[\exp(f_{ca}\bar{\eta})f_{ca}\tilde{\eta} + \frac{\bar{c}_{O_2}}{c^0_{O_2}}\exp(-f_{cc}\bar{\eta})f_{cc}\tilde{\eta} - \frac{\tilde{c}_{O_2}}{c^0_{O_2}}\exp(-f_{cc}\bar{\eta})\right] \quad (25)$$

Prescribed potential boundary conditions for the AC equations are only required for the electronic potential:

$$\tilde{\Phi}_{ELE}\big|_{\text{cathode current collector}} = -\Delta\tilde{\Phi}_0 \qquad \tilde{\Phi}_{ELE}\big|_{\text{anode current collector}} = +\Delta\tilde{\Phi}_0 \quad (26)$$

where $\Delta\tilde{\Phi}_0$ is the perturbation amplitude. Neumann boundary conditions apply everywhere else for the electronic potential, and everywhere for the ionic potentials.

2.2.2.2. AC mass transport. In order to solve for the oscillatory concentrations we need another set of equations to be solved simultaneously with Eqs. (22)–(25). The decomposition shown in Eq. (17) can be applied to the mass balance equations, in a similar way as shown for the charge balance. The equation describing the distribution of hydrogen concentration at the anode can be calculated starting with the general form of the mass balance within the pores at the anode:

$$\frac{\partial c_{H_2}(\bar{x},t)}{\partial t} = D_{H_2-H_2O}\nabla^2 c_{H_2}(\bar{x},t) - \frac{S_{ANO}i_{0,ANO}}{2F}\left[\frac{c_{H_2}(\bar{x},t)}{c^0_{H_2}}\exp(f_{aa}\eta(\bar{x},t)) - \frac{c_{H_2O}(\bar{x},t)}{c^0_{H_2O}}\exp(-f_{ac}\eta(\bar{x},t))\right] \quad (27)$$

Here, the concentration and the overpotential depend on time t and on the spatial coordinates $\bar{x} = (x, y)$. Replacing them using the expressions (17):

$$\frac{\partial(\bar{c}_{H_2} + \tilde{c}_{H_2}\,e^{j\omega t})}{\partial t} = D_{H_2-H_2O}\nabla^2(\bar{c}_{H_2} + \tilde{c}_{H_2}\,e^{j\omega t}) - \frac{S_{ANO}i_{0,ANO}}{2F} \times \left[\frac{\bar{c}_{H_2} + \tilde{c}_{H_2}\,e^{j\omega t}}{c^0_{H_2}}\exp(f_{aa}(\bar{\eta} + \tilde{\eta}\,e^{j\omega t})) - \frac{\bar{c}_{H_2O} + \tilde{c}_{H_2O}\,e^{j\omega t}}{c^0_{H_2O}}\exp(-f_{ac}(\bar{\eta} + \tilde{\eta}\,e^{j\omega t}))\right] \quad (28)$$

After simplification, Eq. (28) results:

$$j\omega\tilde{c}_{H_2} = D_{H_2-H_2O}\nabla^2\tilde{c}_{H_2} - \frac{S_{ANO}i_{0,ANO}}{2F} \times \left[\frac{\bar{c}_{H_2}}{c^0_{H_2}}\exp(f_{aa}\bar{\eta})f_{aa}\tilde{\eta} + \frac{\bar{c}_{H_2O}}{c^0_{H_2O}}\exp(-f_{ac}\bar{\eta})f_{ac}\tilde{\eta} + \frac{\tilde{c}_{H_2}}{c^0_{H_2}}\exp(f_{aa}\bar{\eta}) - \frac{\tilde{c}_{H_2O}}{c^0_{H_2O}}\exp(-f_{ac}\bar{\eta})\right] \quad (29)$$

The derivation of the AC equation for oxygen concentration on the cathode side is slightly more complicated, because of the presence of the extra term in the expression for the oxygen flux (Eq. (14), second term on the r.h.s.). Revisiting Eq. (15),

$$N_{O_2} = \frac{-D_{O_2-N_2}\nabla c_{O_2}}{1-(RT/p)c_{O_2}} \quad (15)$$

it is apparent that we cannot directly incorporate the AC terms as before, because of the presence of the variable in the denominator. However, it is possible to expand the $1/(1-(RT/p)c_{O_2})$ term in a geometric series around some convenient value for $(RT/p)c_{O_2}$. If the expansion is performed around zero, the following expression holds if we neglect second order terms and higher:

$$\frac{-D_{O_2-N_2}\nabla c_{O_2}}{1-(RT/p)c_{O_2}} \approx -D_{O_2-N_2}\nabla c_{O_2}\left(1 + \frac{RT}{p}c_{O_2}\right), \quad (30)$$

as long as $|(RT/p)c_{O_2}| < 1$. Usually, the cathode gas is air, and for air this inequality always holds, since the maximum value it can take is $|(RT/p)c_{O_2}| = 0.21$. The point around which the expansion is centred does not have to be zero, but it can also be, for example, some average oxygen concentration along the cathode channel. If this is the case, the linearization of the expression on the right hand side of Eq. (15) is, for a given intermediate concentration $c^*_{O_2}$:

$$\frac{-D_{O_2-N_2}\nabla c_{O_2}}{1-(RT/p)c_{O_2}} \approx -D_{O_2-N_2}\nabla c_{O_2} \times \left[\left(1-\frac{RT}{p}c^*_{O_2}\right)^{-1} + \left(1-\frac{RT}{p}c^*_{O_2}\right)^{-2} \times \left(\frac{RT}{p}c_{O_2} - \frac{RT}{p}c^*_{O_2}\right)\right] \quad (31)$$

A sensitivity analysis of the results revealed that the choice of intermediate concentration has a negligible effect on the solution, with a maximum discrepancy in value of the left and right hand sides of Eq. (31) varying from 5% when $c^*_{O_2} = 0$–7% when $c^*_{O_2} = 0.21$. Our choice was to expand the term around atmospheric oxygen concentration $(RT/p)c^*_{O_2} = 0.21$, corresponding to a common operating condition of high excess oxidant stoichiometry, resulting in:

$$\frac{-D_{O_2-N_2}\nabla c_{O_2}}{1-(RT/p)c_{O_2}} \approx -D_{O_2-N_2}\nabla c_{O_2}\left[A_1 + A_2\frac{RT}{p}c_{O_2}\right], \quad (32)$$

where $A_1 = 0.929$ and $A_2 = 1.602$. Now, substituting $c_{O_2} = \bar{c}_{O_2} + \tilde{c}_{O_2} e^{j\omega t}$ as before:

$$-D_{O_2-N_2}\nabla c_{O_2}\left[A_1 + A_2\frac{RT}{p}c_{O_2}\right] = -D_{O_2-N_2}\nabla(\bar{c}_{O_2} + \tilde{c}_{O_2} e^{j\omega t})\left[A_1 + A_2\frac{RT}{p}(\bar{c}_{O_2} + \tilde{c}_{O_2} e^{j\omega t})\right] \quad (33)$$

Expanding this expression, reorganizing the time dependent and the time independent terms, and neglecting second order terms, the term on the l.h.s. in Eq. (30) is:

$$-D_{O_2-N_2}\left[A_1 + A_2\frac{RT}{p}\bar{c}_{O_2}\right]\nabla\tilde{c}_{O_2} - e^{j\omega t}D_{O_2-N_2} \times \left[A_1\nabla\tilde{c}_{O_2} + A_2\frac{RT}{p}\bar{c}_{O_2}\nabla\tilde{c}_{O_2} + A_2\frac{RT}{p}\tilde{c}_{O_2}\nabla\tilde{c}_{O_2}\right] \quad (34)$$

The first term in expression (34) is the steady-state (DC) first-order approximation of the term inside the divergence in Eq. (16) multiplied by the effective binary diffusion coefficient. When we combine expression (34) with the other terms that constitute the mass balance for oxygen in (16), the first term in expression (34) vanishes because it is part of the steady state solution, similarly to the case of Eq. (17) in the anode mass balance. The remaining AC terms form the AC mass balance for oxygen in the cathode.

$$j\omega\,\tilde{c}_{O_2} = D_{O_2-N_2}\nabla\cdot\left[A_1\nabla\tilde{c}_{O_2} + A_2\frac{RT}{p}(\bar{c}_{O_2}\nabla\tilde{c}_{O_2} + \tilde{c}_{O_2}\nabla\bar{c}_{O_2})\right] + \frac{S_{CAT}i_{0,CAT}}{4F}\left[\exp(f_{ca}\bar{\eta})f_{ca}\tilde{\eta} + \frac{\bar{c}_{O_2}}{c^0_{O_2}}\exp(-f_{cc}\bar{\eta})f_{cc}\tilde{\eta} - \frac{\tilde{c}_{O_2}}{c^0_{O_2}}\exp(-f_{cc}\bar{\eta})\right] \quad (35)$$

Comparing Eqs. (35) and (29), it can be concluded that the second term inside the first set of brackets of Eq. (35) represents the influence of the unreacting nitrogen on the oxygen flux.

The boundary conditions used for the AC concentrations are:

$\tilde{c}_{H_2} = 0$ at the channel/anode boundary
$\nabla\tilde{c}_{H_2}\cdot n = 0$ everywhere else
$\tilde{c}_{O_2} = 0$ at the channel/cathode boundary
$\nabla\tilde{c}_{O_2}\cdot n = 0$ everywhere else

2.3. Calculation of the cell impedance

Solving for the potentials throughout the modeled domain allows the calculation of the corresponding current densities, using Ohm's law:

$$\begin{aligned} i^{DC}_{ION} &= -k_{ION}\nabla\Phi^{DC}_{ION} \\ i^{DC}_{ELE} &= -k_{ELE}\nabla\Phi^{DC}_{ELE} \\ i^{AC}_{ION} &= -k_{ION}\nabla\Phi^{AC}_{ION} \\ i^{AC}_{ELE} &= -k_{ELE}\nabla\Phi^{AC}_{ELE} \end{aligned} \quad (36)$$

Last, the impedance results from the relationship between the imposed AC perturbation potential and the resulting AC current density.

$$Z(\omega) = \frac{2\Delta\Phi^{AC}}{i^{AC}_{ELE}(\omega)\big|_{\text{current collector}}} \quad (37)$$

Table 1
Operating conditions and geometry used for typical simulations in this work

Property	Value
Temperature, T	850 °C
Operating point, V_{CELL}	0.7 V
Anode channel hydrogen partial pressure, pH^0_2	0.97 atm
Anode channel water partial pressure, pH_2O^0	0.03 atm
Cathode channel oxygen partial pressure, pO^0_2	0.21 atm
Open circuit potential, OCV	1.13 V
Electrolyte thickness, t_{ELY}	150 μm
Anode thickness, t_{ANO}	40 μm
Cathode thickness, t_{CAT}	40 μm
Rib width	2 mm
Channel width	2 mm

2.4. Model parameters

An adequate choice of input parameters is of great importance in the development of numerical models. A nonlinear, convoluted electrochemical system such as a full SOFC is a good example of this statement. Many important system parameters are very difficult, or impossible, to measure independently. Exchange current, transfer coefficients, symmetry factors, tortuosity, and interfacial double-layer capacitance, are examples of these quantities. In addition, the porous nature of the electrodes in a fuel cell further complicates the analysis, since many of their properties are not defined by a single value, but by a distribution of values. Finally, the experimental difficulties inherent to high temperature solid-state electrochemical systems make validation of modeling results extremely difficult. Among these difficulties, contact resistance, system inductance, reference electrode placement, and precursor powder contamination, are examples of external sources of error that hinder accuracy and repeatability. The influence of inaccuracies in the input parameters on the present model results are discussed in Part II of this series. Table 1 shows the operating conditions and geometries used for the simulations.

Model parameters can be classified into three groups, according to the physical process that they characterize:

1. Electrical conductivity
2. Gas species diffusion

Table 2
Electrical conductivity and related properties

Property	Symbol	Value	Ref.
Electrolyte ionic conductivity @ 850 °C	$k_{ION,ELY}$	0.04 S cm^{-1}	[27,28]
Anode bulk electronic conductivity @ 850 °C	$k^{b}_{ELE,ANO}$	1.90×10^4 S cm^{-1}	[29,30]
Cathode bulk electronic conductivity @ 850 °C	$k^{b}_{ELE,CAT}$	2.66×10^2 S cm^{-1}	[28]
Anode porosity volume fraction	ε_{ANO}	0.4	This work
Cathode porosity volume fraction	ε_{CAT}	0.4	This work
Anode electronically conductive phase volume fraction[a]	$x_{ELE,ANO}$	0.4	This work
Cathode electronically conductive phase volume fraction[a]	$x_{ELE,CAT}$	0.5	This work
Anode ionically conductive phase volume fraction[a]	$x_{ION,ANO}$	0.6	This work
Cathode ionically conductive phase volume fraction[a]	$x_{ION,CAT}$	0.5	This work
Interconnect conductivity @ 850 °C	$k_{ELE,IC}$	8.0×10^3 S cm^{-1}	[31]

[a] Based on total solid phase.

3. Electrochemistry

2.4.1. Electrical conductivity

Table 2 shows bulk conductivities and volume fractions of the materials used for the electrodes, electrolyte, and interconnect.

The calculation of conductivity in porous electrodes requires a correction for the presence of non-conducting phases. The approach used in this work is the one used by Kenney and Karan [18], approximating the probability of percolation with the volume fraction of the corresponding phase, as presented in detail in [19]:

$$\sigma_k^{\text{eff}} = (1 - \varepsilon) \cdot x_k \cdot P(x_k)\sigma_k^{\text{bulk}}$$

Here the effective conductivity of phase k, σ_k^{eff}, depends on the porosity ε, the volume fraction of phase k in the solid phase, x_k, and the probability of percolation P.

The large electronic conductivity of the electrodes and the interconnect makes them practically equipotential. The ionic conductivity of the electrodes is one of the factors that influence the extent of penetration of the electrochemical reaction from the electrolyte interface into the electrode volume.

2.4.2. Gas species diffusion

The effective diffusivity in porous media is smaller than the bulk diffusivity, and it can be calculated using a correction analogous to that of conductivity. Unlike the case of electrical conductivity, there is reasonable consensus on the type of correction to use:

$$D^{\text{eff}} = \frac{\varepsilon}{\tau} D^{\text{bulk}},$$

where ε and τ are the porosity and tortuosity of the pore phase, respectively. Despite the relative agreement on the functional form of the diffusivity correction, the tortuosity value is still a source of discrepancy. The magnitude of the tortuosity depends on both the total level of porosity and on the microstructural morphology. Typical values for tortuosity reported in the literature range from 2 to 7, and sometimes reach as high as 10 [20]. A dedicated study [21] was recently published stating that $\tau = 3$ is a reliable estimate for SOFC electrodes based on tortuosity measurements, and that is the value used in the simulations in this work. As far as the bulk diffusivities are concerned, they can be calculated using the Lennard–Jones formulation [22]. Their values, and the corresponding effective values, are summarized in Table 3.

2.4.3. Electrochemistry

Factors affecting the rate of the electrochemical reactions at the SOFC electrodes include electroactive surface area, exchange current density, and charge transfer coefficients. The AC behavior is characterized by the capacitance of the electrochemical double-layer existing at the interfaces. The nature and details of the reactions taking place at a microscopic level in SOFCs remain largely unknown, and one reason for this limitation is the difficulty to directly measure the electrochemical parameters mentioned above. From a modeling viewpoint, it is necessary to make estimates based on fitting model results to experimental data. A problem inherent to electrode-level modeling of 3D electrodes is the indirect relationship between what can be measured and what has to be modeled. When measuring a polarization curve or an impedance spectrum, the quantities that are accessible to the measurement are the current and potentials *at the current collectors*. It is not possible to measure current

Table 3
Gas diffusion properties

Property	Symbol	Value	Ref.
Hydrogen bulk diffusivity in H_2–H_2O @ 850 °C		8.9 cm^2 s^{-1}	[22]
Oxygen bulk diffusivity in O_2–N_2 @ 850 °C		2.3 cm^2 s^{-1}	[22]
Anode and cathode porosity	ε_{ANO}, ε_{CAT}	0.4	This work
Anode and cathode tortuosity	τ_{ANO}, τ_{CAT}	3	[21]
Hydrogen effective diffusivity in H_2–H_2O @ 850 °C	$D_{H_2-H_2O}$	1.2 cm^2 s^{-1}	This work
Oxygen effective diffusivity in O_2–N_2 @ 850 °C	$D_{O_2-N_2}$	0.3 cm^2 s^{-1}	This work

Table 4
Anode and cathode experimental data used to calculate the exchange current and the double layer capacitance by fitting

Property and conditions	Symbol	Value	Ref.
Cathode polarization resistance @ OCV, 3-electrode measurement, 850 °C	Rp	~0.8 Ω cm^2	Fig. 8a in [32]
Cathode summit frequency @ OCV, 2-electrode measurement, 850 °C	fp	~0.5 Hz	Fig. 8a in [32]
Anode polarization resistance @ OCV, 2-electrode measurement, 850 °C, 97%H_2, 3% H_2O	Rp	0.4 Ω cm^2	Fig. 5.4 in [30]
Anode summit frequency, 3-electrode measurement, 850 °C	fp	3600 Hz[a]	Fig. 4 in [33]

[a] Data not available at OCV, but taken at 300 mA cm^{-2}.

Table 5
Electrochemical data adopted from the literature and results of the fitting

Property	Symbol	Value	Ref.
Anode charge transfer coefficient, anodic direction	α_{AA}	1.2	[34]
Anode charge transfer coefficient, cathodic direction	α_{AC}	0.8	[34]
Cathode charge transfer coefficient, anodic direction	α_{CA}	1.5	[28,35]
Cathode charge transfer coefficient, cathodic direction	α_{CC}	0.5	[28,35]
Anode and cathode active surface area	S_{ano}, S_{cat}	10^6 m^{-1}	[25]
Anode volumetric exchange current density	S_{ano} $i_{0,ano}$	2.5×10^7 A m^{-3}[a]	[30]
Cathode volumetric exchange current density	S_{cat}, $i_{0,cat}$	5×10^7 A m^{-3}[a]	[32]
Anode double layer capacitance @ 850 °C	$C_{dl,ano}$	0.4 F m^{-2}[a]	Fig. 4 in [33]
Cathode double layer capacitance @ 850 °C	$C_{dl,cat}$	90 F m^{-2}[a]	Fig. 8a in [32]

[a] Fitted to reproduce empirical impedance results.

density *within the electrode volume*. Therefore, the relationship between, e.g., a measured exchange current and i_0 in Eq. (3) and similar ones, is not straightforward. A similar situation occurs with the observed charge transfer coefficients, as recently shown in [23] and [18]. Patterned electrode experiments are useful in trying to measure electrochemical parameters on a simple geometry [24], and provide evidence of the inverse relationship between polarization resistance and triple-phase-boundary length, reflected in this model as the electroactive surface area. It is clear, then, that the products Si_0 and SC_{dl} are to be considered together as volumetric exchange current and volumetric double layer capacitances, and whose values need to be adjusted to fit relevant experimental data.

The procedure adopted in the present work is as follows. Charge transfer coefficients were adopted from published results on single electrode studies at the modeled temperature. Surface areas were estimated based on a published model that uses particle size and packing theory [25]. The exchange current density and the double layer capacitance are then the only free parameters at each electrode, tuned to match published apparent polarization resistance and peak frequency determined by impedance spectroscopy performed in single electrode experiments. Tables 4 and 5 summarize these data.

3. Results and discussion

3.1. Intact cell

Figs. 2 and 3 show examples of the results obtained with the model, for a cell with no degradation. Fig. 2 shows the electronic current density magnitude and distribution within the interconnect material. The figure on the right shows contour lines of equal current density, with the numbers indicating the current density magnitude in A cm^{-2}, and the figure on the left shows the corresponding streamlines. Close to the electrode the current density lines curve toward the channel because of partial oxygen starvation underneath the interconnect rib. Fig. 3 shows the oxygen concentration within the porous electrodes. Underneath the interconnect rib, reactant access is limited by diffusion, and the concentration is much lower than below the channel, especially in the cathode. The reactant starvation underneath the interconnect rib has important performance implications. Localized depletion limits the electrochemical activity within the porous electrode because of the dependence of kinetics on reactant concentration. Fig. 4 shows the difference in perfor-

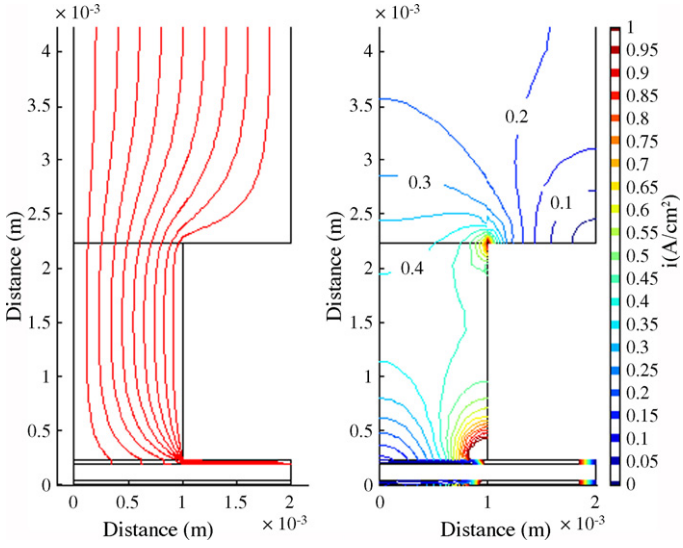

Fig. 2. Electronic current density magnitude contours (right, numbers indicate A cm^{-2}), and corresponding streamlines (left), at the cathode current collector for an intact cell, working at 0.7 V. Close to the cell the current density lines bend toward the channel because of oxygen starvation underneath the interconnect rib. Axes labels indicate length in metres.

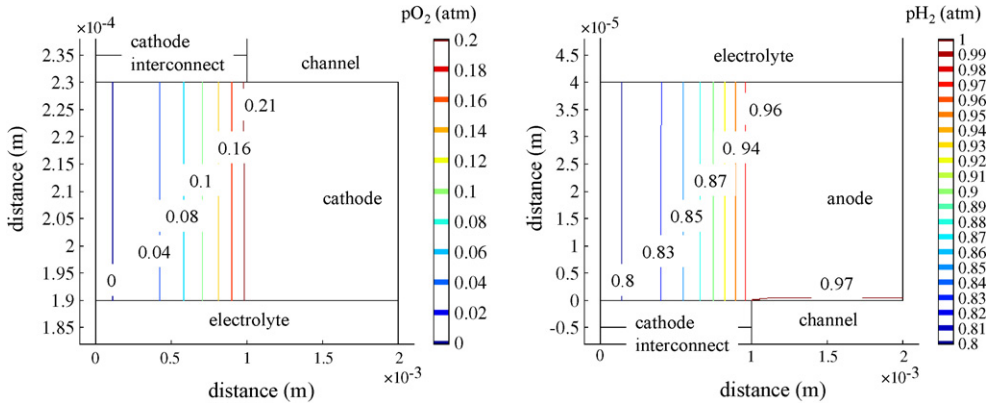

Fig. 3. Reactant partial pressure contour lines inside the porous cathode (left) and anode (right), in atm. The limited access of reactant to regions underneath the interconnect rib causes local depletion. Note the difference in the color scale ranges. The pictures show half of the rib width and half of the channel width for symmetry. Axes indicate length in metres.

mance between the cell presented in this work and an equivalent cell with no interconnect. Although both simulations used the same electrochemical and diffusional parameters, the performance of the cell that includes the interconnect is lower due to localized reactant depletion. Fig. 5 shows the Nyquist plot of the resulting impedance, with two arcs related to the cell electrochemistry at high (anode) and low (cathode) frequency, plus one related to the anode diffusion behavior, at an intermediate frequency. The size of the electrochemistry related arcs depend on kinetics and on reactant concentration at both electrodes. The anode diffusional arc depends on rib size and on the anode gas diffusivities, as determined by numerical experiments in which each of the parameters was varied one at a time.

In practice, the ability to distinguish the electrode arcs depends on the difference in their characteristic relaxation frequencies. If these frequencies are similar, the impedance plot would show two convoluted arcs adding up to the same total polarization resistance. The identification of interface contact degradation mechanisms, however, can be performed even when the arcs are convoluted, as will be shown later.

3.2. Cell with contact degradation

3.2.1. Cathode delamination

A thin layer of elements with the dielectric characteristics of air inserted between the cathode and the electrolyte simulates a delamination at this interface. The effect of cathode delamination is essentially the same as that previously reported for the button cell geometry in [4]. The regions affected by delamination become electrochemically inactive. No current is generated within the electrode volume directly above and below the delamination. Fig. 6 illustrates this statement, showing that the electronic current density is negligible in the regions affected by delamination. An observation of Fig. 6 reveals:

1. The almost total deactivation of the affected zone, both on the cathode (top) side, and on the anode (bottom) side, with

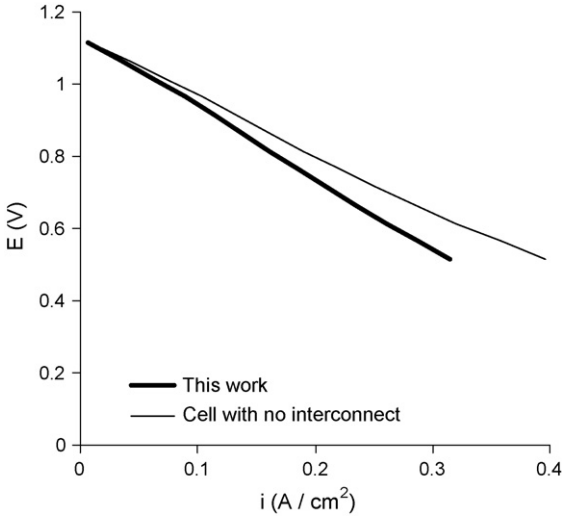

Fig. 4. Polarization curve corresponding to the intact cell including the ribbed interconnect (thick line), compared with the equivalent polarization curve for a cell (thin line) with no interconnect, modeled using the same kinetic parameters. The ribbed interconnect lowers the overall performance by limiting the access of reactant in regions underneath the ribs.

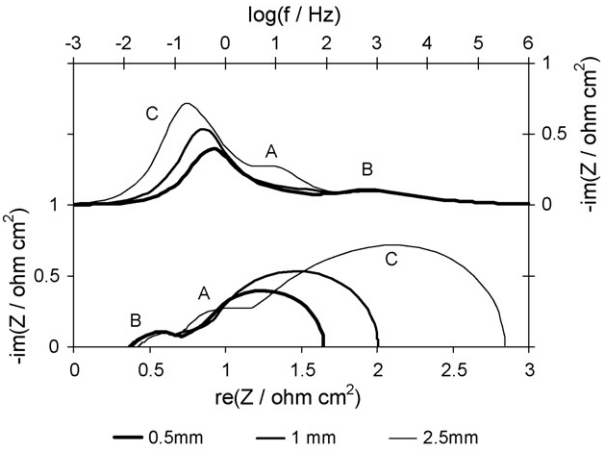

Fig. 5. Impedance corresponding to an intact cell, for three different rib widths. Arc A is a result of the anode diffusional limitation, increasing in size for larger rib widths. Processes B and C correspond to anodic and cathodic electrochemical reactions, respectively. Legend labels indicate rib and channel half-width.

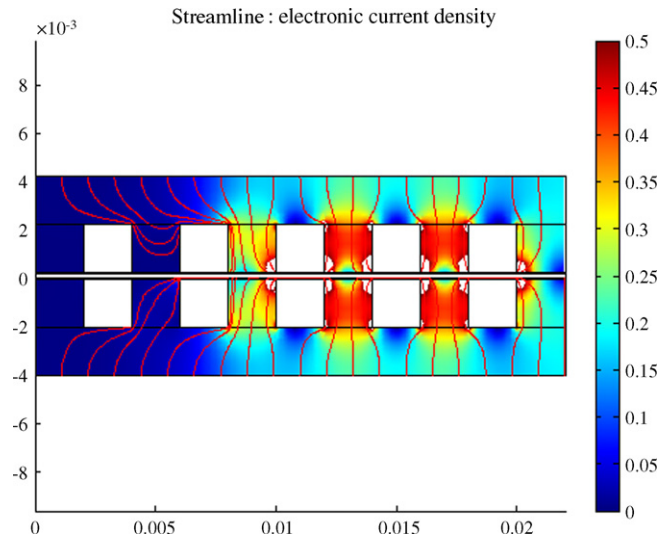

Fig. 6. Electronic current density magnitude (color scale, A cm^{-2}) and streamlines after occurrence of a delamination between the cathode and the electrolyte extending for a length of 2 rib and 2 channel widths. Axes indicate spatial dimensions in meters. The zone affected by delamination is deactivated.

delamination occurring at the cathode–electrolyte interface. This is the result of the cell shadowing due to its high aspect ratio.

2. The third rib from the left (above an intact portion of the cell) carries less current than it does when the entire cell is intact, because the cathode segment under the second channel from the left is inactive and does not generate any demand for charge carriers.
3. The intact rib adjacent to the delamination does not take up any current from its neighbors above the delamination. This observation contrasts with the case presented in Section 3.2.3, constituting a distinct difference between delamination and interconnect detachment.

Cathode delamination affects the impedance similarly as it does for a cell with the same geometry but with no interconnect, with a simultaneous and equivalent increase in both series and

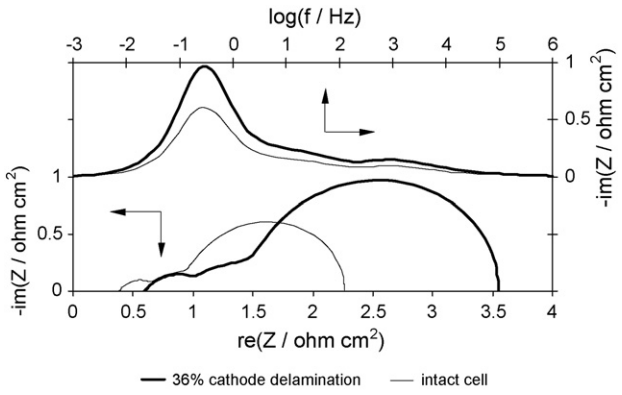

Fig. 7. Impedance change caused by a cathode delamination of length two ribs and two channels. While series (high frequency intercept) and polarization (arc size) resistances increase, the peak frequencies remain unchanged.

polarization resistances and no change in peak frequencies, as shown in Fig. 7. The reason for this behavior is the shadowing caused by the large cell aspect ratio. Although delamination may appear at first glance to be an inherently ohmic phenomenon, it effectively reduces the size of the cell's projected area, by an amount equal to the area of the delamination. The number of reaction sites is decreased by an amount proportional to the delaminated area, thereby increasing the polarization resistance by decreasing the overall electrochemical activity of the cell. This result demonstrates the inter-relation between series and polarization resistances, two quantities usually assumed independent of each other.

This behavior provides further evidence of the need for an alternative to the equivalent circuit model to understand delamination, because the equivalent circuit analogy, being inherently 1-dimensional, cannot explain a change in arc size without a change in peak frequency if the electrochemistry remains unaltered.

In summary, the ohmic resistance increase and the electrochemical deactivation produced by electrode delamination results in the series and polarization resistance increasing simultaneously and equivalently as delamination progresses. This

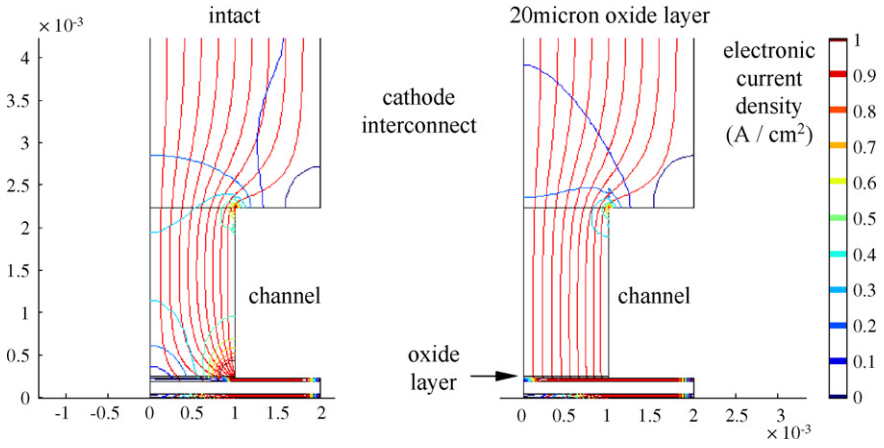

Fig. 8. Electronic current density magnitude contours (scale, A cm^{-2}), and corresponding streamlines (red), at the cathode current collector for the intact case (left), and for a cell with a 20 μm thick chromium oxide layer between the interconnect and the cathode (right). (For interpretation of the references to color in this figure legend, the reader is referred to the web version of the article.)

event is likely to occur during thermal cycling (typically cathode delamination) or redox cycling (anode delamination), rather than continuously in time.

3.2.2. Oxide layer growth between the interconnect and the cathode

A chromium oxide layer that grows between the interconnect rib and the cathode hinders the flow of electrons into the electrode and, consequently, degrades the cell performance by increasing its overall resistance. This phenomenon is simulated in the present model by inserting a layer of elements with the conductivity of chromia between the interconnect and the cathode. Fig. 8 shows the current density magnitude and distribution after the growth of a 20 μm thick oxide layer between the interconnect and the cathode. This thickness corresponds to the extrapolation of the oxidation kinetics data presented in [7] and [9] to 40,000 h, the target lifetime of a stationary SOFC. The current density is much lower than it was in the intact case (Fig. 2), and there is no significant curvature of the current lines. Fig. 9 shows the change in impedance for this degradation mode. The thin line curve shows the impedance for the intact case, for comparison. The increase in series resistance is approximately 0.4 Ω cm^2. For a thickness of 20 μm, and an electronic conductivity of Cr_2O_3 of 0.01 S m^{-1} at 850 °C, this increase represents twice the value:

$$R^{\Omega} = \frac{\delta}{\sigma} = \frac{\text{thickness}}{\text{conductivity}}$$

because the interconnect rib surface on which the layer grows is half as wide as the total unit width. Another noticeable feature of the post degradation spectrum is the slight increase in polarization resistance. This behavior is related to the dependence of polarization resistance on the overall cell polarization. In potentiostatic mode, the change in overall series resistance introduced by the oxide layer lowers the total current density. This change produces a change in polarization resistance, especially of the cathode. The nonlinear dependence of overpotential on current density implies that the polarization resistance of an electrode is also current density dependent. This behavior has been reported in an earlier modeling report by Zhu and Kee [26, Fig. 6]. Part II revisits this and other interaction phenomena.

3.2.3. Rib detachment between the interconnect and the cathode

Another degradation mechanism involving the interconnect plates is the loss of contact, or detachment, of one or more ribs with the electrode. Analogously to the case of delamination, a layer of elements with the conductivity of air simulates the interfacial detachment, this time between the interconnect plate and the cathode. In common with oxide layer growth, this problem causes an increase in the total resistance of the cell, but it is physically of a different nature. Fig. 10 shows the redistribution of the electronic current density after the detachment of the first two interconnect ribs, on the cathode side, from the left. The electronic current density increases substantially at the first intact rib adjacent to the group of detached ribs, since the cell underneath the interconnect detachment is still electrochemically active. This increased local current density could lead to further degradation because of localized overheating. Fig. 11 shows the impact of interconnect detachment on the cell impedance. Similarly to oxide layer growth, interconnect detachment has the largest effect on series resistance, with practically no change in characteristic frequency. However, interconnect detachment does have an effect on polarization resistance (Fig. 12, solid triangles), in contrast with oxide layer growth. The reason is the non-negligible shadowing effect caused by the increase in the electronic current path length around the detachment. Unlike electrode delamination [4], interconnect detachment degrades the cell performance by blocking electronic species. The high mobility of the electrons makes the performance loss caused by this degradation mode less severe than that caused by electrode delamination. In the case of electrode delamination, the blocking

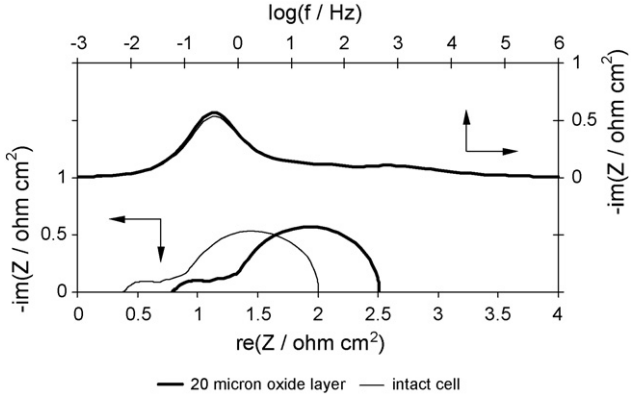

Fig. 9. Impedance change after the growth of a 20 μm oxide layer between the cathode and the interconnect. The series resistance increases by about 0.4 Ω cm^2. The characteristic frequencies remain practically unaltered. The intact case is shown as a thin line for comparison. Calculation made using the half-rib/half-channel repeating unit. The polarization resistance in the intact case is slightly lower than in the examples using the 6-rib interconnect geometry because the repeating unit does not show end effects related to more severe reactant starvation under the end ribs.

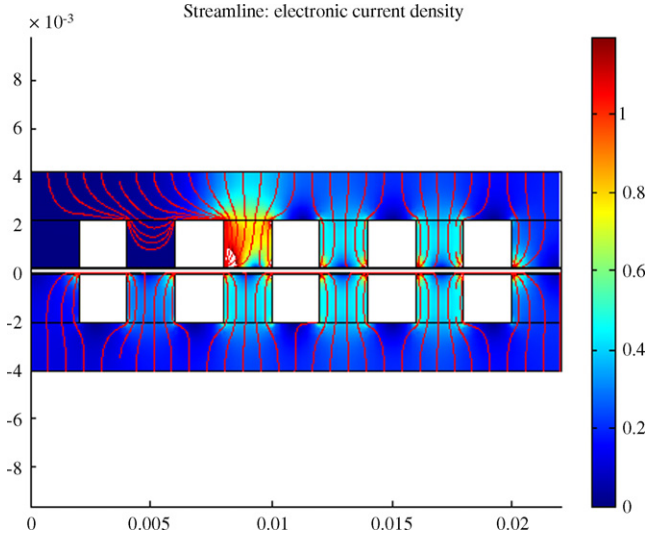

Fig. 10. Redistribution of the electronic current density upon the detachment of the first two interconnect ribs on the cathode side. The current density increases at the first intact rib. Unlike the case of electrode delamination (Fig. 6), the electrochemical activity on the bottom side is not obliterated, but lowered.

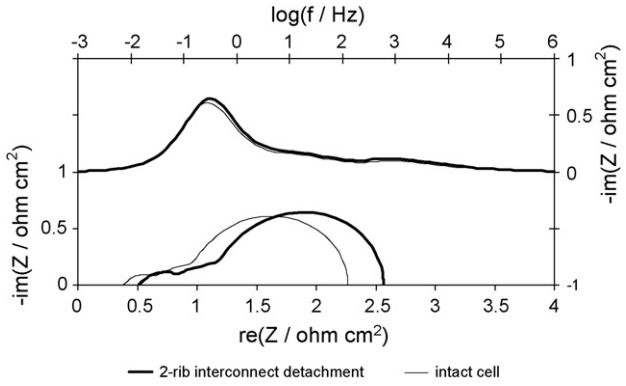

Fig. 11. Impact of interconnect rib detachment on the impedance spectrum. The reduction of the conduction area increases the series resistance. The high electronic conductivity of the electrodes redistributes the current density, thereby limiting the shadowing effect on polarization resistance.

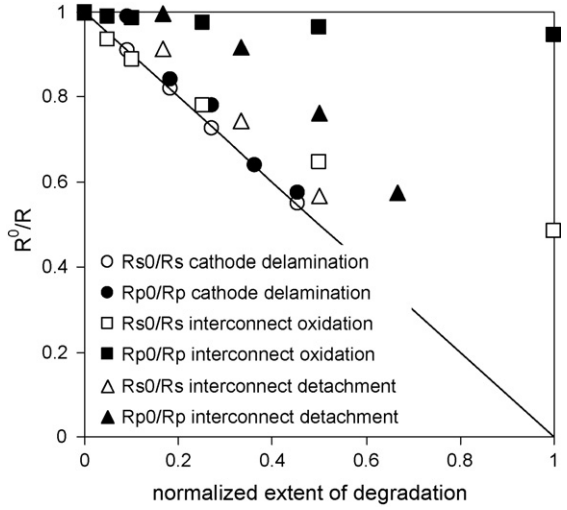

Fig. 12. Normalized resistance trends for all degradation cases considered. Open symbols: normalized series resistance. Filled symbols: normalized polarization resistance.

of ionic species deactivates the affected area since ions cannot readily travel the long path around the delamination due to their limited mobility.

3.3. Normalized resistance

One useful way to characterize the trend followed by the impedance upon the occurrence of progressive degradation consists of analyzing the normalized series and polarization resistances:

$$\bar{R}_S = \frac{R_S^0}{R_S} \quad \bar{R}_P = \frac{R_P^0}{R_P}$$

In this way, these variables range from one to zero, corresponding to the intact and totally destroyed cases, respectively. Plotting these variables as a function of a normalized quantity associated with the extent of degradation can give useful insight on what type of degradation is affecting the cell. Examples of such abscissa variables include fraction of active area lost due to electrode delamination [4], and fraction of total active area lost due to microstructural degradation [14]. Although the extent of degradation is not a quantity that is known in practice for an operating cell, the normalized series and polarization resistances can be tracked as a function of time, possibly showing a distinct behavior that can be used for identification purposes.

Applying this concept to oxide layer growth is not straightforward, since "total" degradation cannot be defined for a progressively increasing oxide layer thickness. To circumvent this problem, we defined the "total" degradation oxide layer thickness as the thickness corresponding to 40,000 h of operation, based on a growth kinetic study reported in the literature at the temperature of operation simulated in the present work: approximately 20 μm, at 0.1 $\mu m\,h^{-0.5}$ [7]. A conductivity of 0.01 $S\,cm^{-1}$ was used for Cr_2O_3 at 850 °C.

Fig. 12 shows the normalized resistances for all degradation modes under study, as a function of extent of degradation, defined as:

Degradation mode	Extent of degradation
Delamination	Delamination length/total length
Oxide layer growth	Oxide layer thickness/20 μm
Interconnect detachment	Detachment length/total length

The trend in normalized resistance is different for all three cases.

While delamination affects series and polarization resistance to the same extent and simultaneously, oxide layer growth mainly affects series resistance. Interconnect detachment affects series resistance to a larger extent than it affects polarization resistance. The shadowing effect of detachment only becomes evident for large extents of degradation, at which in-plane electronic conduction becomes limiting. The trend in normalized resistances is then a further potential tool for degradation diagnosis, in addition to impedance peak tracking.

The concept of normalized resistance is also useful to study the influence of design parameters on how degradation affects cell performance. The effect of interconnect rib size on performance loss caused by interconnect oxidation is an example of this statement. Interconnect oxidation mainly degrades the cell performance by increasing its series resistance. Therefore, it is expected that the interconnect/electrode area ratio will have an influence on how cell performance deteriorates as the oxide layer builds up at the interconnect surface. The next two sections describe the influence of design parameters on resistance increase for interconnect oxidation and interconnect detachment.

3.3.1. The effect of interconnect geometry on resistance increase caused by interconnect oxidation

The choice of rib and channel size in planar SOFCs responds to a compromise between adequate electronic conductivity from cell to cell, and good reactant diffusion from the flow channel into the porous electrode. Fig. 13 (left) compares the results obtained in Section 3.2.2 for the default interconnect geometry (rib = channel = 2 mm) with a larger (5 mm), and a smaller (1 mm) geometry, indicating that the results are nearly independent of interconnect geometry for the case where rib and channel

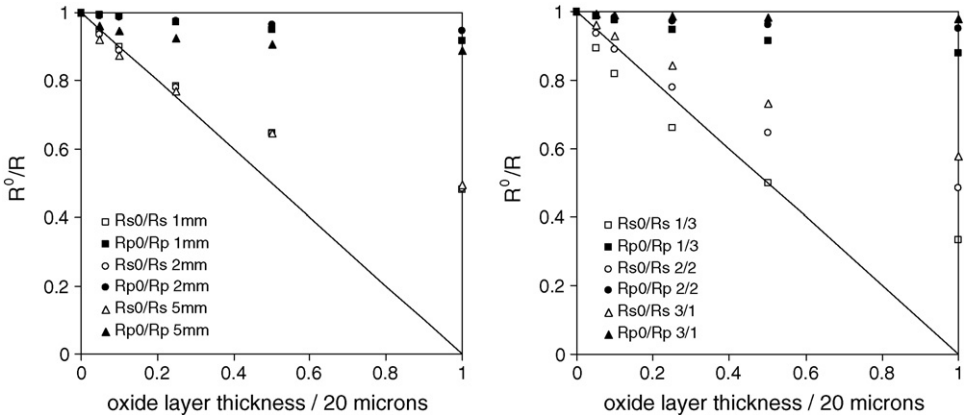

Fig. 13. Left: The effect of interconnect rib and channel widths on the normalized resistances for oxide layer growth, for the case of equal width. Right: The effect of interconnect rib and channel width on the normalized resistances for oxide layer growth, for the case of total width equal to 4 mm. Fractional numbers in the label indicate rib/channel width in mm. The series resistance increases to a larger extent, the narrower the rib.

are of equal size. In contrast, Fig. 13 (Right) shows that the series resistance is more severely affected for narrow rib sizes, for the case of a constant rib + channel total width of four millimetres. This result is of importance in designing interconnect flow fields. It demonstrates that the performance of the cell over the full design lifetime, including any changes resulting from degradation over the lifespan, should be considered in the initial flowfield design, and not only the reactant supply and current collection in the initial stages of the stack life.

The performance loss associated with oxide layer growth on the interconnect increases with oxide layer thickness, as expected. The increase in series resistance depends only on the layer thickness, and its effect will be much more severe, in relative terms, in high performance cells, compared to low performance cells. In contrast, electrode delamination causes the same relative loss of performance for a given amount of delaminated area. Small rib width/channel width ratios show good performance in the intact state due to beneficial reactant and product diffusion effects, but they are more severely influenced by oxide layer growth than cells with large relative rib width.

3.3.2. *The effect of interconnect geometry on resistance increase caused by interconnect detachment*

Fig. 14 (left) shows the effect of interconnect geometry on the results for rib detachment. For equally wide ribs and channels, the relative deterioration is larger for wider ribs and channels, as seen in the graph on the left. For rib and channel of constant total rib + channel width (Fig. 14, right, equal to 4 mm in this example), the relative deterioration is larger for narrower ribs and wider channels, as shown in the graph on the right. It is important to take into account that the normalized resistance value provides information about the relative deterioration, rather than real cell performance.

3.4. *Computational requirements*

Fig. 1 (main) and Fig. 1 (inset) are the two geometries considered in the present work. The possibility to use the simplified geometry (Fig. 1, inset) depends on the degradation mode under consideration, and in particular, on its influence on the cell symmetry. The only degradation mode reported in this work that does not modify the overall symmetry of the problem is inter-

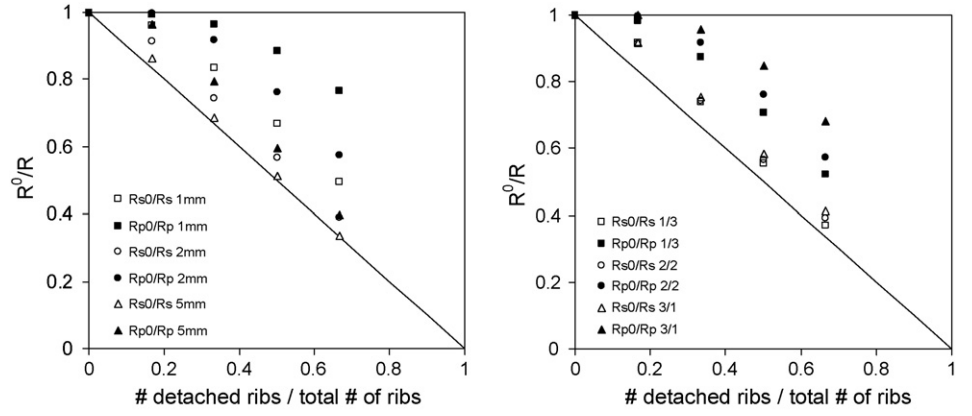

Fig. 14. Influence of rib/channel width on the relative performance loss upon detachment of an increasing number of interconnect ribs. Left: Ribs and channels of equal width: 1 mm, 2 mm, and 5 mm. Relative deterioration increases with increasing width. Right: Constant rib + channel width equal to 4 mm. Fractional numbers in the label indicate rib/channel width in mm. Relative deterioration increases with narrower ribs and wider channels.

Table 6
Computational demand for each intact case considered

Geometry	# DoF	Problem	# iter	Time (s)	
Full, ASC	36945	DC (nonlinear)	2	8	–
	36945	AC (linear)	–	606	61 freq
Full, ESC	32361	DC (nonlinear)	2	7	–
	32361	AC (linear)	–	476	61 freq
Simplified, ASC	9951	DC (nonlinear)	2	2.6	–
	9951	AC (linear)	–	139	61 freq
Simplified, ESC	7491	DC (nonlinear)	2	2.2	–
	7491	AC (linear)	–	92.1	61 freq

Full geometry: Fig. 1. Simplified geometry: Fig. 1 (*inset*).

connect oxidation, since the assumption is that all rib/cathode interfaces are affected identically. Electrode delamination and interconnect detachment, on the other hand, drastically modify the overall current path, destroying left-to-right symmetry, and demanding the modeling of the entire geometry. Thus, the computational demand of these two geometries varies greatly.

The model was solved using quadrilateral Lagrangian elements. Interfaces and corners require special attention, since it is at those places where variables show large gradients. A combination of MATLAB and COMSOL resulted very useful for the numerical implementation of the model. In this way, it is easier to vary any aspect of the model, including the geometry, without the need to use a graphical user interface that would require redrawing the whole problem for every case. More importantly, it is important to code the meshing strategy in such a way that it adapts to changes in the geometrical characteristics of the system, thereby increasing the method's efficiency at the expense of relinquishing the convenience of automatic meshing algorithms.

Table 6 summarizes the data corresponding to the problem size (i.e. DoF = degrees of freedom) and computational time. For each case (DC and AC), the system solves for four unknown functions: ionic and electronic potentials, and hydrogen and oxygen concentration. The computer used in the simulation had an Intel® Pentium® 4 CPU with 1 GB RAM.

4. Conclusions

A comprehensive two-dimensional SOFC model that simulates both steady state and AC behavior was presented to study the effect of contact degradation modes on the impedance spectrum. This work expands the two-dimensional model of a full SOFC presented previously to include the ribbed interconnect plates and examines the effect of contact degradation modes related to the interconnect plates. Even in the intact case, the presence of the ribbed interconnect influences the overall cell performance by hindering the access of reactant to regions underneath the ribs, thereby locally decreasing the electrochemical activity. This is the first report of an SOFC impedance model that includes the interconnect plates.

Electrode delamination degrades both conductivity and electrochemistry in an SOFC. It constitutes a direct hindrance to the flow of charge between the electrodes, and also deactivates the cell everywhere in the electrodes above and below the delaminated zone as a result of the large aspect ratio of the cell. This deactivation effectively shadows the cell over the affected area. The simultaneous and equivalent increase in series and polarization resistances, proportional to the delaminated area, is a distinct change of the impedance spectrum that may be used for identification purposes. Since it does not cause a change in the electrochemical processes, delamination is expected to leave the relaxation frequencies of the electrochemical processes unchanged.

Interconnect oxidation is an important degradation mode affecting contact resistance. This degradation mode mainly affects performance by increasing the SOFC series resistance. The extent of degradation increases for small rib/channel width ratios. A small change in the electrode arcs may appear as a consequence of the polarization resistance dependence on overall current density, but this contribution is small compared with the change in ohmic resistance. The characteristic frequency of the electrode arcs remains essentially unchanged.

The simulation of interconnect detachment yielded interesting results in terms of the physical difference between interconnect detachment and electrode delamination. The loss of performance resulting from detachment is less severe than that caused by delamination, since electrons, the blocked species, can move laterally in the electrodes to a much larger extent than ions can move within the electrolyte. Consequently, this mechanism produces an increase in series resistance, with some increase in polarization resistance, with almost no peak frequency change.

Tracking the change in normalized series and polarization resistance provides further useful information on the type of degradation affecting the cell. Part II of this work further exploits the benefits of this concept by describing the influence of simultaneous degradation modes on the SOFC impedance.

References

[1] E. Ivers-Tiffée, Q. Weber, D. Herbstritt, J. Eur. Ceram. Soc. 21 (2001) 1805–1811.
[2] R. Barfod, M. Mogensen, T. Klemensoe, A. Hagen, Y. Liu, Proc. SOFC IX 1 (2005) 524–533.
[3] A. Hagen, R. Barfod, P. Hendriksen, Y. Liu, Proc. SOFC IX 1 (2005) 503–513.
[4] J.I. Gazzarri, O. Kesler, J. Power Sources 167 (2) (2007) 430–441.
[5] T. Iwata, J. Electrochem. Soc. 143 (5) (1996) 1521–1525.
[6] J. Bentzen, Bilde-Soerensen, Y. Liu, M. Mogensen, Proc. 26th Risoe International Symposium on Materials Science, Roskilde, Denmark, 2005, pp. 127–132.
[7] J.-H. Park, K. Natesan, Oxidation Met. 33 (1–2) (1990) 31–53.
[8] D. Larrain, J. van Herle, D. Favrat, J. Power Sources 161 (2006) 392–403.
[9] T. Brylewski, et al., Solid State Ionics 143 (2001) 131–150.
[10] P. Huczkowski, et al., Fuel Cells 06 2 (2006) 93–99.
[11] X. Chen, et al., Solid State Ionics 176 (5–6) (2005) 425–433.
[12] K. Huang, P. Hou, J. Goodenough, Solid State Ionics 129 (2000) 237–250.
[13] J. Malzbender, T. Wakui, R.W. Steinbrech, Proceedings of the Sixth Euro. SOFC Forum, vol. 1, 2004, pp. 329–338.
[14] J.I. Gazzarri, O. Kesler, J. Power Sources 167 (1) (2007) 100–110.
[15] F. Zhao, T. Armstrong, A. Virkar, J. Electrochem. Soc. 150 (2003) A249.
[16] J. Welty, C. Wicks, R. Wilson, G. Rorrer, Fundamentals of Momentum, Heat, and Mass Transfer, fourth ed., John Wiley and Sons, 2001, p. 428.
[17] B. Tribollet, J. Newman, J. Electrochem. Soc. 131 (12) (1984) 2780–2785.
[18] B. Kenney, K. Karan, J. Electrochem. Soc. 153 (6) (2006) A1172–A1180.

[19] A. Ioselevich, A. Kornyshev, W. Lehnert, Solid State Ionics 124 (1999) 221–237.
[20] P. Costamagna, K. Honegger, J. Electrochem. Soc. 145 (1998) 3995.
[21] R. Williford, L. Chick, G. Maupin, S. Simner, J. Stevenson, J. Electrochem. Soc. 8 (150) (2003) A1067–A1072.
[22] J. Welty, C. Wicks, R. Wilson, G. Rorrer, Fundamentals of Momentum, Heat and Mass Transfer, fourth ed., John Wiley & Sons, 2001, p. 432.
[23] J. Soderberg, A. Co, A. Sirk, V. Birss, J. Phys. Chem. B 110 (2006) 10401–10410.
[24] R. Radhakrishnan, A. Virkar, S. Singhal, J. Electrochem. Soc. 152 (1) (2005) A210–A218.
[25] P. Costamagna, P. Costa, V. Antonucci, Electrochim. Acta 43 (3–4) (1998) 375–394.
[26] H. Zhu, R. Kee, J. Electrochem. Soc. 153 (9) (2006) A1765–A1772.
[27] S. Singhal, K. Kendall (Eds.), High-temperature Solid Oxide Fuel Cells: Fundamentals, Design and Applications, Elsevier, Oxford, 2003, p. 73.
[28] B. Kenney, K. Karan, Proceedings of Hydrogen and Fuel Cells, 2004, pp. 1–11.
[29] D. Pollock, Physical Properties of Materials for Engineers, second ed., CRC Press, 1993, p. 210.
[30] R. Stübner, Untersuchungen zu den Eigenschäften der Anode der Festoxid-Brennstoffzelle (SOFC), Ph.D. Thesis, 2002, p. 24.
[31] S. Loo, Abs. 1150, 204th Meeting, The Electrochemical Society, 2003.
[32] M. Jørgensen, M. Mogensen, J. Electrochem. Soc. 148 (5) (2001) A433–A442.
[33] S. Primdahl, M. Mogensen, J. Appl. Electrochem. 30 (2000) 247–257.
[34] M. Gonzalez-Cuenca, "Novel anode materials for solid oxide fuel cells", Ph.D. Thesis, Univ. Twente, 2002.
[35] F. van Heuveln, H. Bouwmeester, J. Electrochem. Soc. 144 (1997)134–139.